Journal of Materials Chemistry A

ROYAL SOCIETY OF CHEMISTRY

PAPER

View Article Online
View Journal | View Issue

Cite this: J. Mater. Chem. A, 2020, 8, 4911

Atom-precise incorporation of platinum into ultrafine transition metal carbides for efficient synergetic electrochemical hydrogen evolution†

Xingxing Pan,[a] Shuanglong Lu,[*a] Duo Zhang,[b] Ye Zhang,[c] Fang Duan,[a] Han Zhu,[a] Hongwei Gu,[d] Shuao Wang[b] and Mingliang Du[*a]

Received 17th November 2019
Accepted 3rd February 2020

DOI: 10.1039/c9ta12613a

rsc.li/materials-a

Exploring highly efficient and stable electrocatalysts for the hydrogen evolution reaction (HER) has captured widespread attention. Atomic engineering of material structures paves a powerful pathway to develop advanced electrocatalysts by virtue of precisely modulating the reactivity and maximizing the atomic efficiency, although it still stands as a big challenge. In this work, a new method of multiple molecular level confinement is proposed to *in situ* incorporate atomic platinum (1.5 wt%) into ultrafine transition metal carbides through electrospinning and pyrolysis. The hybrid catalyst exhibits superior electrocatalytic performance towards the HER in acidic medium in terms of overpotential (38 mV at 10 mA cm^{-2}), Tafel slope (27 mV dec^{-1}), mass activity (3.49 A mg^{-1}) and stability (10 mV decay after 5000 CV cycles). Detailed investigation reveals that the excellent performance is mainly attributed to the electronic modulation of atomic Pt over α-MoC_{1-x} and highly exposed active sites originating from atomic and ultrafine properties. The generality of this method is further demonstrated with a Pt-doped ultrafine WC_x catalyst. This work elucidates a facile strategy to design efficient electrocatalysts *via* atomic nanostructure and composition engineering, shedding light on the exploration and optimization of hybrid catalysts.

Introduction

Hydrogen has been considered as one of the most promising sources of clean energy to substitute traditional fossil fuels.[1,2] To enable efficient and massive production of hydrogen, electrochemical water splitting driven by highly active electrode catalysts has drawn intensive attention due to its flexibility and convenience.[3,4] Typically, platinum-based catalysts, having excellent catalytic activity and corrosion resistance, are the most extensively utilized electrode catalysts for the hydrogen evolution reaction (HER) at the cathode.[5] However, the high cost and limited reserves of precious platinum present a huge barrier to its widespread use, which severely limits the real practical applications.[6–8] Therefore, it is highly required to dramatically decrease the use of platinum or develop low-cost alternatives without compromising the catalytic activity and stability towards hydrogen production.

In the past decade, transition metals[9,10] and their carbides,[11,12] nitrides,[13,14] chalcogenides,[15,16] phosphides[17,18] have gained broad research interest due to their high activity, excellent stability and earth abundance. Particularly, transition metal carbides (TMCs), which feature a noble-metal-like electronic configuration and high electronic conductivity, have emerged as a promising catalyst candidate towards the HER.[19] Since the first paper discovering the HER activity of molybdenum carbide was published by Vrubel and Hu,[20] remarkable advances have been made through structural design or electronic modulation of TMCs.[21] Accordingly, two methods are typically used to enhance their catalytic performance. One of the effective strategies is nanostructure engineering or carbon immobilization to increase the number of active sites.[22,23] Another method relies on heteroatom doping or heterostructure engineering to increase the intrinsic activity.[24–26] In this regard, developing a facile method, which not only modulates the electronic structure,[27,28] but also maximizes the active sites,[29,30] is desirable for further boosting the HER performance of TMCs. However, the catalytic activity reported for these newly

[a]Key Laboratory of Synthetic and Biological Colloids, Ministry of Education, School of Chemical and Material Engineering, Jiangnan University, Wuxi, 214122, China. E-mail: lushuanglong@jiangnan.edu.cn; du@jiangnan.edu

[b]State Key Laboratory of Radiation Medicine and Protection, School of Radiation Medicine and Protection, Collaborative Innovation Center of Radiation Medicine of Jiangsu Higher Education Institutions, Soochow University, Suzhou, 215123, China

[c]International Collaborative Laboratory of 2D Materials for Optoelectronics Science and Technology of Ministry of Education, Institute of Microscale Optoelectronics, Shenzhen University, Shenzhen, 518060, China

[d]Key Laboratory of Organic Synthesis of Jiangsu Province, College of Chemistry, Chemical Engineering and Materials Science, Collaborative Innovation Centre of Suzhou Nano Science and Technology, Soochow University, Suzhou, 215123, China

† Electronic supplementary information (ESI) available: SEM, HR-TEM, LSV plots, Tafel plots, durability tests, XRD, EIS, CV, Raman spectra, elemental mapping images and comparison of the HER performance with other electrocatalysts. See DOI: 10.1039/c9ta12613a

discovered TMC-based HER alternatives is still far from that of Pt-based materials. Considering the practical trials of Ni_3N/Pt,[31] CoS_2/Pt,[32] N–Mo_2C/Pt,[33] $Co(OH)_2$/Pt[34] and Pt/MoN,[35] hybrid catalysts, hybrid catalysts that combine low-cost, noble-metal-like TMCs[36] with low content of Pt, especially atomic Pt, are proposed to provide highly efficient electrocatalytic performance toward the HER. Single atoms or clusters anchored on supports could show maximum atom efficiency and precise electronic modulation,[37,38] which have already been realized in various supports aimed at different reactions. However, it still remains a big challenge to achieve scalable production and exert excellent control over the dispersity.

Inspired by classical coordination chemistry and previous research studies on molecular confined synthesis of single atoms,[39–42] we present here a novel molecular level engineering method. Through combining the strategy of heteropoly acid (HPA) confinement with electrospinning, a hybrid catalyst composed of carbon nanofibers and single atom or cluster Pt doped TMCs is fabricated (Fig. 1). HPAs are very stable precursors for TMCs; they also provide plenty of coordination sites with rich oxygen atoms exposed, which is favorable for the introduction and stabilization of foreign components.[43] To further stabilize the confinement and avoid sintering at high temperature, electrospinning nanofibers, which have been proved in our previous studies as an efficient carbon support for electrocatalysts,[44–46] is introduced to generate highly dispersed ultrafine TMC nanoparticles (NPs) (usually the average size is below 2 nm). Specifically, a commonly used heteropoly acid $H_3PMo_{12}O_{40}$ (PMA) is selected as a model HPA to coordinate with platinum ions.[47] By tailoring the ratios of precursors and the carbonization temperature, a series of carbon nanofibers (CNFs) decorated with an ultralow content of Pt doped α-MoC_{1-x} NPs (Pt/α-MoC_{1-x}-CNFs) were obtained. These atomic Pt doped α-MoC_{1-x} NPs are highly uniform with a narrow size distribution and the doping content of Pt is as low as 1.5 wt%. According to previous research studies, α-MoC_{1-x} exhibits strong interaction with Pt and the similarities in the electronic structures will lead to good adhesion and synergistic catalytic performance.[48] The electron transfer in our case from α-MoC_{1-x} to atomic Pt is also evidenced by EXAFS and XPS spectra. As expected, the optimal hybrid catalyst shows excellent activity and stability towards the HER. The overpotential at a current density of 10 mA cm^{-2} (η_{10}) equals 38 mV in acidic solution, which is close to that of benchmark Pt/C (η_{10} = 30 mV), and the Tafel slope is just 27 mV dec^{-1}. After 5000 cyclic voltammetry (CV) cycles, only 10 mV decay of η_{10} is observed. The greatly enhanced catalytic performance of transition metal carbides with ultra-low Pt doping is further demonstrated with tungsten carbide catalysts, which shows the generality of this design and synthetic method to construct novel hybrid HER catalysts.

Experimental

Chemicals and materials

Platinum bis(acetylacetonate) ($Pt(acac)_2$) was provided by Shanghai Civi Chemical Technology Co., Ltd. Phosphomolybdic acid (PMA), *N*,*N*-dimethylformamide (DMF), ethanol and sulfuric acid (H_2SO_4) were purchased from Sinopharm Chemical Reagent Co., Ltd. Polyacrylonitrile (PAN, MW: 150 000 g mol^{-1}) and Nafion solution (5 wt%) were purchased from Sigma-Aldrich and Aladdin Industrial Co., Ltd respectively. Commercial Pt/C (20 wt%) was obtained from Hesen Co., Ltd. All chemicals were used without further purification. All solutions used in experiments were prepared with deionized water (18.2 MΩ cm).

Synthesis of Pt/α-MoC_{1-x}-CNFs

Typically, 0.2 mmol platinum bis(acetylacetonate) ($Pt(acac)_2$) and phosphomolybdic acid (PMA) were dissolved in 7 mL DMF under constant stirring. Then, 1.0 g polyacrylonitrile (PAN, molecular weight: 150 000) was added at room temperature to obtain a homogeneous solution, followed by the electrospinning process. The as-obtained sticky electrospinning solution was applied under high voltage between the spinneret and the collector at room temperature to fabricate a uniform fiber membrane. The as-collected fiber membrane was dried at 60 °C overnight under vacuum and subsequently transferred into a tube furnace. Then the pyrolysis process was divided into two successive steps. First, a pre-oxidation step was performed at 200 °C in air for 1 h. Second, a carbonization step was performed from 200 °C to over 700 °C under an Ar atmosphere for 3 h to produce carbon nanofibers. The prepared product was labeled Pt/α-MoC_{1-x}-CNFs. Various molar ratios of $Pt(acac)_2$ and PMA (0.2/0.05 to 0.2/0.2) were applied to obtain a series of nanocomposite fibers, denoted as Pt/α-MoC_{1-x}-CNFs-(1 to 4) respectively using the same procedure mentioned above.

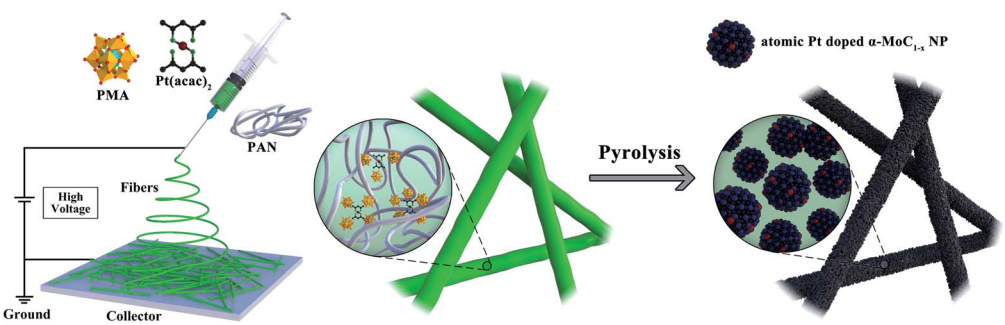

Fig. 1 Schematic illustration for the preparation of Pt/α-MoC_{1-x}-CNFs.

Similarly, nanocomposite fibers were also prepared at different carbonization temperatures (800 °C to 1200 °C), denoted as Pt/α-MoC_{1-x}-CNFs-(800 to 1200) respectively. In order to investigate the influence of different doped amounts of Pt on the HER performances, different molar concentrations of $Pt(acac)_2$ (0.1–0.3 mmol) were used with other conditions unchanged, and the obtained products were denoted as Pt/α-MoC_{1-x}-CNFs-(0.1–0.3) respectively. Pt-CNFs and α-MoC_{1-x}-CNFs were prepared under the same conditions for comparison except for the absence of PMA or $Pt(acac)_2$.

Synthesis of Pt/WC_x-CNFs

Pt/WC_x-CNFs were synthesized using a similar method to that of Pt/α-MoC_{1-x}-CNFs by substituting $H_3PW_{12}O_{40}$ (PTA) for $H_3PMo_{12}O_{40}$ (PMA). The samples with different ratios of $Pt(acac)_2$ and PTA (0.2/0.05 to 0.2/0.15) were denoted as Pt/WC_x-CNFs-(1 to 3), respectively.

Materials characterization

The size and morphology of the as-fabricated products were studied using an S-4800 field-emission scanning electron microscope (FE-SEM) and a JEM-2100 transmission electron microscope (TEM) operated at 3 kV and 200 kV, respectively. High-angle annular dark field scanning transmission electron microscopy (HAADF-STEM) and line-scan energy dispersive X-ray spectroscopy (EDX) were carried out using a STEM (Tecnai G2 F30S-Twin, Philips-FEI) at an acceleration voltage of 300 kV. Atomic Pt atoms were measured by AC HAADF-STEM (Titan3 Themis G2 FEI). X-ray diffraction (XRD) was performed using a Bruker AXSD8 Advance X-ray diffractometer with Cu K_α radiation ($\lambda = 1.5406$ Å) at a scanning rate of 0.02° s^{-1} in the 2θ range of 10–90°. X-ray photoelectron spectroscopy (XPS) was recorded using a scanning X-ray microprobe (ESCALAB 250XI). Binding energy values were referenced to the C 1s binding energy which was taken as 284.8 eV. Raman spectra (LabRAMAramis, Horiba Scientific, 532 nm) were employed to investigate the existence of carbon. The contents of Mo and Pt in the sample were determined by inductively coupled plasma (ICP) analysis. The Pt L_3-edge X-ray absorption fine structure (XAFS) spectra were recorded at the BL14W1 beamline in the Shanghai Synchrotron Radiation Facility (SSRF). The data were obtained in fluorescence mode. Pt foil as the reference sample was applied for energy calibration. The raw data were processed using IFEFFIT software packages according to the standard analysis procedures.

Electrochemical measurements

Electrochemical measurements for the HER were conducted with a CHI660H workstation (Shanghai Chenhua, Shanghai). All experiments were carried out using a conventional three-electrode system in 0.5 M H_2SO_4, where a glassy carbon electrode (GCE, 3 mm in diameter, 0.07065 cm^2) with catalysts was used as the working electrode, a standard $Hg/HgCl_2$ electrode was used as the reference electrode, and a graphite rod was used as the counter electrode for the HER. All potentials were converted to the reversible hydrogen electrode (RHE) according to $E_{RHE} = E_{SCE} + 0.0592 \times pH + 0.2438$. Typically, 3 mg of the catalyst and 80 μL of 5 wt% Nafion solution were dispersed in 1 mL of 3 : 1 v/v water/ethanol by at least 1 h of sonication to form a homogeneous ink. Then 5 μL of the catalyst ink was loaded onto a GCE and dried under ambient conditions. In order to compare the performance of catalysts, the commercial Pt/C modified electrode was prepared in the same way. Linear sweep voltammetry (LSV) was performed at a scan rate of 5 mV s^{-1}. Electrochemical impedance spectroscopy (EIS) spectra were recorded with the frequency ranging from 0.01 to 10^5 Hz at an amplitude of 5 mV. The electrochemical stability of catalysts was tested by sweeping cyclic voltammetry (CV) between 0 and 0.54 V *vs.* the reversible hydrogen electrode (RHE) at a scan rate of 50 mV s^{-1}. The mass activity is normalized to the Pt loading as follows:

$$\text{Mass activity} = \frac{j \times S}{\frac{m}{v} \times v' \times w\%}$$

where j is the current density at a certain overpotential, S is the area of the working electrode, m is the mass of the catalyst, v and v' are the volume of catalyst solution and catalyst ink supported on the electrode, respectively, and w% is the content of Pt in different catalysts by ICP-OES measurement.

Results and discussion

The typical synthesis of hybrid catalysts is schematically illustrated in Fig. 1. Specifically, $Pt(acac)_2$ and PMA were co-electrospun into PAN fibers, following which the fibers were first pre-oxidized under air and then annealed under an Ar atmosphere. The morphology and structure of the as-obtained Pt/α-MoC_{1-x}-CNFs were analyzed and the results are shown in Fig. 2.

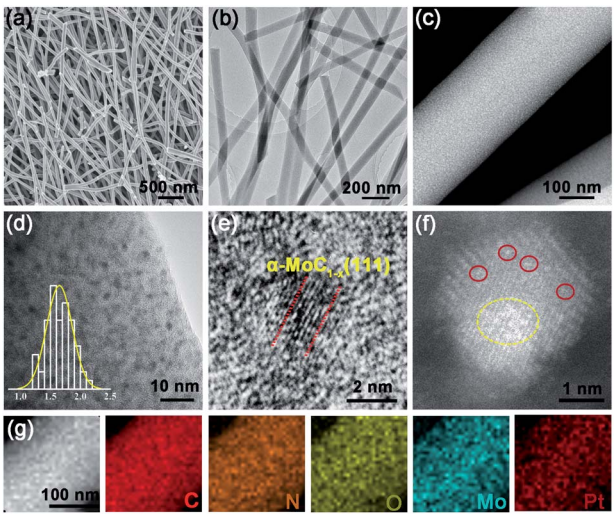

Fig. 2 (a) SEM, (b) TEM, (c) HAADF-STEM and (d) HR-TEM images of Pt/α-MoC_{1-x}-CNFs; the inset in (d) shows the size distribution of α-MoC_{1-x} NPs in the CNF. (e) HR-TEM and (f) aberration-corrected HAADF-STEM images of one single α-MoC_{1-x} NP in the CNFs, with single atoms of Pt marked in red circles and Pt clusters highlighted in yellow. (g) The corresponding elemental mapping of C, N, O, Mo, and Pt in Pt/α-MoC_{1-x}-CNFs.

The uniform fibers (100–150 nm) are evidenced by the low-magnification SEM and TEM images in Fig. 2a and b. The one-dimensional carbon nanofibers are favourable for conductivity and resistance to corrosion. Surprisingly, dense ultrafine nanoparticles (NPs) with a narrow size distribution are decorated throughout the whole carbon nanofiber, as shown in the higher magnification TEM image (Fig. 2d). The average size of these NPs is only 1.65 nm from the statistical counting of 100 randomly picked NPs. The excellent dispersity is further confirmed by HAADF-STEM (Fig. 2c). Such highly dispersed and ultra-small NPs are possibly ascribed to the confinement of carbon fibers, which could increase the exposed active sites, thus helping to improve electrocatalytic performance. The high-resolution TEM image in Fig. 2e identifies a lattice fringe of 0.24 nm, which is assigned to the (111) facet of α-MoC_{1-x}. Pt is possibly doped in the α-MoC_{1-x} NPs, because no lattice fringes of Pt are found in the high-resolution TEM image. To gain deep insight into the surface properties, the aberration-corrected HAADF-STEM image of one single α-MoC_{1-x} NP is shown in Fig. 2f. Clearly, bright dots and domains with atomic size are anchored on the surface of α-MoC_{1-x} without any agglomeration, suggesting that atomically isolated Pt sites were obtained. Furthermore, the EDS mapping analysis in Fig. 2g confirms that the main composition of C, N, O, Mo and Pt elements is well dispersed on the nanofibers, indicating the uniform elemental distribution in the CNFs. The exact Pt and Mo contents in the Pt/α-MoC_{1-x}-CNFs were determined to be 1.50 wt% and 10 wt%, respectively, by ICP-OES measurement.

Through the analysis of the XRD pattern, the phase of Mo in the hybrid catalyst is ascertained as α-MoC_{1-x} (JCPDS no. 89-2868) (Fig. 3a). Four main characteristic diffraction peaks at approximately 37.36°, 42.43°, 62.0° and 75.12° are identified, corresponding to the (111), (200), (220) and (311) facets of the face-centered-cubic (fcc) α-MoC_{1-x} phase, respectively, which is consistent with the HR-TEM image and that reported in ref. 49. The diffraction peaks of α-MoC_{1-x} are broad, proving the ultrafine property of the as-formed α-MoC_{1-x} NPs, as also evidenced by the TEM characterization. No diffraction peaks of metallic Pt can be found in the XRD pattern, illustrating that the size of Pt is too small to be detected by the XRD measurement. These results are in accordance with the HR-TEM, HAADF-STEM and ICP results. All the evidence above further confirms the assumption that Pt is atomically doped in α-MoC_{1-x} NPs, which originates from the effective confinement of PMA through the electrospinning and pyrolysis process.

The atomic Pt dopant is proposed to modulate the surface electronic state of α-MoC_{1-x} NPs. To confirm the modulation, XPS of Pt/α-MoC_{1-x}-CNFs was conducted. As depicted in the full XPS spectrum (Fig. 3b), Pt/α-MoC_{1-x}-CNFs are mainly constituted of C, N, O, Mo and Pt elements and a low atom content of Pt is observed (0.28 at%). The high resolution XPS spectrum of C 1s (Fig. 3c) shows four pronounced peaks centered at 289.2, 285.7, 285.0 and 284.8 eV, which correspond to C=O, C–O, C–N and C=C species, respectively. The peak of C 1s at around 284.8 eV reveals a high degree of graphitization, which may contribute to providing excellent electron transfer properties. The N 1s spectrum in Fig. 3d displays triple splits (graphitic N, 401.15 eV;

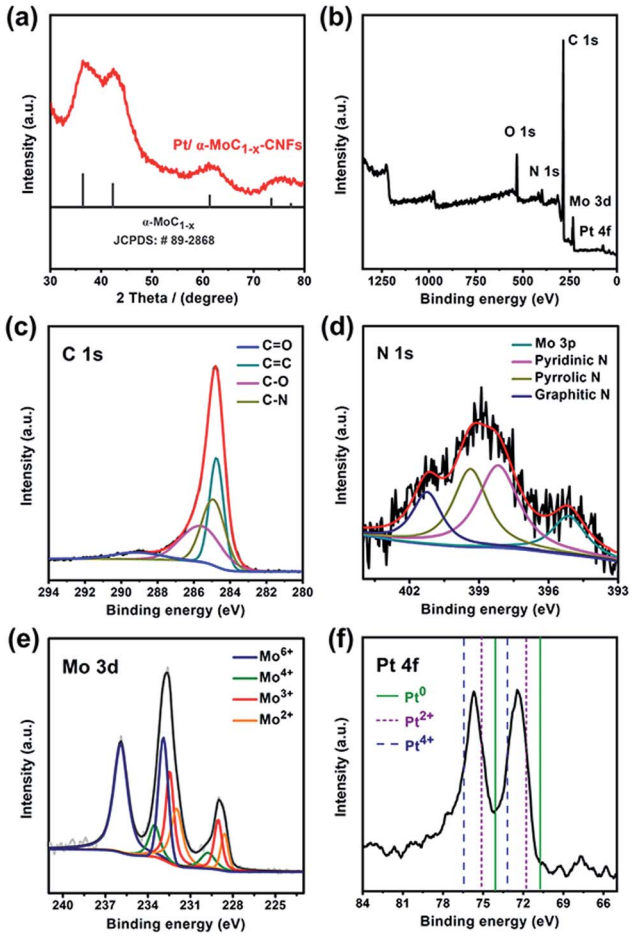

Fig. 3 (a) XRD spectra of Pt/α-MoC_{1-x}-CNFs. (b) Low-resolution XPS spectrum of Pt/α-MoC_{1-x}-CNFs. High-resolution XPS spectra of Pt/α-MoC_{1-x}-CNFs: (c) C 1s, (d) N 1s, (e) Mo 3d and (f) Pt 4f.

pyrrolic N, 399.35 eV; pyridinic N, 398.2 eV) and a slight overlap with Mo 3p (observed at 395.15 eV),[50,51] which is commonly found in PAN derived carbon nanofibers and Mo-containing carbon materials. Three strong peaks of Mo 3d, centered at 235.9, 232.6, and 229 eV, are observed in Fig. 3e. The peak fitting of Mo 3d profiles indicates that there are four electronic states (+2, +3, +4, and +6) for Mo on the surface of Pt/α-MoC_{1-x} NPs. The Mo^{6+} (235.9 and 232.9 eV) and Mo^{4+} (233.5 and 229.8 eV) species resulting from inactive MoO_3 and MoO_2 are commonly considered as oxidized species when molybdenum carbides are exposed to air. Mo^{2+} and Mo^{3+}, commonly recognized as electrocatalytically active centers in molybdenum carbides,[28] are located at 232.0/228.6 eV and 232.5/229.0 eV, respectively. These results suggest that Mo in PMA is transformed into α-MoC_{1-x} species *via* pyrolysis. Two XPS peaks of Pt 4f (Fig. 3f) located at 75.7 and 72.4 eV correspond to Pt $4f_{5/2}$ and Pt $4f_{7/2}$, respectively. The oxidation state of Pt is between +4 and +2 and close to +2, indicating that Pt is oxidized after being doped in α-MoC_{1-x} NPs. Such a phenomenon could be attributed to the possible strong interaction between Pt atoms and α-MoC_{1-x}.

The electronic structure of Pt in Pt/α-MoC_{1-x} was further investigated by X-ray absorption near-edge spectroscopy

(XANES), as displayed in Fig. 4a. The comparison of the Pt L_3-edge XANES spectra with those of Pt foil and PtO_2 indicates that the white line intensity of Pt in Pt/α-MoC_{1-x} is between those of Pt foil and PtO_2, which suggests the positive charge oxidation state of Pt.[52] This observation is consistent with XPS results. To elucidate the Pt local chemical environment in Pt/α-MoC_{1-x}, extended X-ray absorption fine structure (EXAFS) was carried out. The k_3-weighted Fourier transform of Pt L_3-edge of EXAFS spectra (Fig. 4b) for Pt in Pt/α-MoC_{1-x} displays a dominant peak located at 1.60 Å, lower than the Pt–O distance (1.66 Å) in PtO_2, which is possibly ascribed to the contribution of Pt–C bonding. Moreover, the weak Pt–Pt peak (2.61 Å) is detected, the intensity of which is much lower than the peak of Pt foil. The above results are consistent with structural characterization that Pt single atoms or clusters were atomically doped in the α-MoC_{1-x} NPs. The electron transfer between Pt and Mo was further evidenced by XPS comparisons. Meanwhile, α-MoC_{1-x}-CNFs and Pt-CNFs were obtained under the same conditions except for the addition of a Mo precursor or Pt precursor. As shown in Fig. 4c, the Mo 3d spectrum of Pt/α-MoC_{1-x}-CNFs was also deconvoluted into four doublets for Mo^{2+}, Mo^{3+}, Mo^{4+} and Mo^{6+}, respectively. Carefully checking the peak area reveals a noticeable increase of Mo^{6+} species and a decrease of Mo^{2+}, Mo^{3+} and Mo^{4+} species in Pt/α-MoC_{1-x}-CNFs in comparison with bare α-MoC_{1-x}-CNFs. This phenomenon is consistent with the positively charged Pt as shown in Fig. 3f. These results demonstrate more oxidized Mo and reduced Pt states in Pt/α-MoC_{1-x}-CNFs,[49,53] which originate from the electron transfer from Mo to Pt in Pt/α-MoC_{1-x}-CNFs. These results match well with the morphology characterization. Interestingly, nanoparticles in α-MoC_{1-x}-CNFs and Pt/α-MoC_{1-x}-CNFs show similar dispersity and size distribution (Fig. S1e and f†). The electrospinning fiber provides an ideal confinement for the Mo phase transformation from PMA precursor into the MoO_x intermediate and finally ultrafine α-MoC_{1-x} NPs. More importantly, the introduction of Pt does not change the uniform distribution property of α-MoC_{1-x} NPs. When the PMA is absent, bigger and uneven sized Pt NPs are observed on the CNFs (Fig. S1d†), revealing the effective stabilization of PMA over Pt ions through the electrospinning and pyrolysis process.

Further investigation of the ability of PMA in confining Pt ions was conducted under similar synthetic conditions by varying the molar ratios of $Pt(acac)_2$ and PMA (Fig. S2 and S4†). As shown in Fig. S2a,† when 0.05 mmol PMA was introduced into the electrospinning precursor, large sized Pt NPs almost disappeared during the identical fabrication process, while ultrafine but sparse NPs emerged instead. With further increase of PMA, the NPs have a trend to become denser and denser (Fig. S2a–d†), until an obvious aggregation was observed when the amount of PMA reached 0.2 mmol (Fig. S2d†). Screening all trials, no big sized Pt NPs were detected in the TEM images. Among them, Pt/α-MoC_{1-x}-CNFs-2 (0.1 mmol PMA) shows optimal dispersion of highly dense ultrafine MoC_{1-x} NPs. The dense catalytic sites without aggregation are conducive to maximize the catalytic activity. In addition to the number of catalytic sites, the phase of Mo also changed during the input variation of PMA. In the XRD spectra (Fig. S3†), all diffraction peaks become stronger and sharper as the content of PMA increased, indicating the increased amount of nanostructural α-MoC_{1-x}. Afterwards, the characteristic peak of metallic Mo at 40.53° (ref. 54) is detected in the XRD pattern along with the continuous increase of PMA. Excessive PMA precursor led to the appearance of metallic Mo mainly caused by the non-abundant carbon in the carbon fibers. Compared with bare α-MoC_{1-x} synthesized under the same conditions, four characteristic peaks, ascribed to (111), (200), (220) and (311) of α-MoC_{1-x} with Pt doping, show a slight shift to a higher diffraction angle, which suggests that the lattice parameters of α-MoC_{1-x} decrease after doping Pt into the lattice. The insertion of Pt atoms in the α-MoC_{1-x} lattice is proposed to modulate the electronic state, which has been proved in the XPS analysis.

With the optimal molar ratios of $Pt(acac)_2$ and PMA in hand, the carbonization temperature is expected to exert a great influence on the quality of CNFs and crystallinity of NPs. With the increase of carbonization temperature, there is a distinct trend for α-MoC_{1-x}, changing from clusters with low crystallinity to NPs with a concrete grain boundary, which is also accompanied by a slight increase in the size of α-MoC_{1-x} NPs (Fig. S5a–e†). The crystallinity evolution is further proved by the XRD pattern (Fig. S6†). The metastable fcc α-MoC_{1-x} phase emerged when the carbonization temperature was increased to 1000 °C, evidenced by the intensity increase of typical peaks. The metastable property and moderate crystallinity of the α-MoC_{1-x} phase at 1000 °C are proposed to immobilize Pt atoms more easily. Raman measurements were then conducted to investigate the degree of graphitization of the CNFs at different carbonization temperatures. In Fig. S7,† two peaks at around 1360 cm^{-1} and 1602 cm^{-1} are detected, which are ascribed to the D band and G band, respectively. The sharp D and G peaks indicated a high graphitization degree of carbon, which could improve the conductivity of catalyst materials. As evaluated from the intensity ratios, the I_D/I_G value of Pt/α-MoC_{1-x}-CNFs-2 is decreased slightly with increasing temperature, indicating that the carbonization temperature here has a slight influence on the graphitization degree of CNFs.

This is the first time such ultrafine and highly dispersed α-MoC_{1-x} NPs with atomic Pt doping have been demonstrated. The present synthetic strategy enables us to fabricate novel hybrid catalysts. For one thing, compared with previously

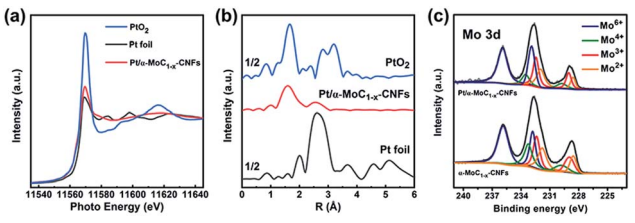

Fig. 4 (a) Normalized XANES spectra at the Pt L_3-edge of Pt foil, PtO_2 and Pt/α-MoC_{1-x}-CNFs. (b) The k_3-weighted Fourier transform of EXAFS spectra derived from XANES of Pt foil, PtO_2 and Pt/α-MoC_{1-x}-CNFs. *R* is the interatomic distance. (c) Mo 3d spectra of Pt/α-MoC_{1-x}-CNFs and α-MoC_{1-x}-CNFs.

reported research studies for the preparation of TMCs, the electrospinning method provides an ideal platform to confine the growth of TMCs, which is favorable to control the size of NPs. A facile *in situ* hybridization of TMCs with conductive CNFs is achieved through the process. For another, HPA, providing plenty of coordination sites for Pt ions with rich oxygen atoms exposed, is chosen as the precursor for TMCs. The Pt atoms are separated and localized by HPA, leading to the effective atomic doping of Pt in TMCs after the pyrolysis. The facile and efficient *in situ* synthesis, as well as the structural superiority of atomic Pt doped ultrafine α-MoC_{1-x} NPs on carbon nanofibers, has great advantages over recently reported two-step synthesis of α-MoC_{1-x} supported Pt NPs.[49,55]

Due to the morphology and electronic properties, the as-obtained catalyst is supposed to have superior HER performance. The electrocatalytic activity of Pt/α-MoC_{1-x}-CNFs, α-MoC_{1-x}-CNFs, Pt-CNFs and commercial Pt/C (Alfa, 20 wt%) was explored in an acidic electrolyte. Fig. 5a presents LSV curves of all samples with IR-drop corrections. Although the α-MoC_{1-x} NPs are highly dispersed with ultrafine diameters, the bare α-MoC_{1-x}-CNFs delivered inferior hydrogen evolution activity. Impressively, the atomic Pt dopant exerts great influence on activity and Pt/α-MoC_{1-x}-CNFs show a notable decrease in the overpotential to achieve a current density of 10 mA cm^{-2} (η_{10}). Among all the electrospun samples, Pt/α-MoC_{1-x}-CNFs-2 shows the best performance with a low η_{10} = 38 mV, which is comparable to that of state-of-the-art commercial Pt/C (η_{10} = 30 mV), significantly better than that of Pt-CNFs (η_{10} = 348 mV), α-MoC_{1-x}-CNFs (η_{10} = 318 mV), Pt/α-MoC_{1-x}-CNFs-1 (η_{10} = 104 mV), Pt/α-MoC_{1-x}-CNFs-3 (η_{10} = 59 mV) and Pt/α-MoC_{1-x}-CNFs-4 (η_{10} = 73 mV). The differences in polarization curves clearly highlight the beneficial effects of atomic Pt doping and the optimal amount of PMA precursors used. The amount of Pt doping is assumed to exert an influence on the HER performance. Different molar concentrations of $Pt(acac)_2$ were then applied in the starting materials and the corresponding polarization curves of the derived catalysts are shown in Fig. S8.† Apparently, when $Pt(acac)_2$ is decreased to 0.1 mmol, an obvious performance decay is observed. If $Pt(acac)_2$ is increased to 0.3 mmol, its catalytic activity at higher current density outperforms that of the optimal Pt/α-MoC_{1-x}-CNFs. To gain a deep insight into the mechanism, the corresponding Tafel slopes ($\eta = b \log j + a$, in which b is the Tafel slope and j is the current density) are calculated and the curves are shown in Fig. 5b. Pt/α-MoC_{1-x}-CNFs-2 presents Pt-like kinetics with a Tafel slope of 27 mV dec^{-1}, which is close to that of commercial Pt/C, proving faster HER kinetics following the Tafel slope determined from the Volmer–Tafel mechanism. The double-layer capacitance (C_{dl}), which is relative to the electrochemically active surface area (ECSA), has been evaluated from the CVs with various scan rates (Fig. S9a–e†). As shown in Fig. S9f,† the C_{dl} of Pt/α-MoC_{1-x}-CNFs-2 is 1.07 mF cm^{-2}, larger than that of other catalysts, indicating its larger ECSA. As the carbonization temperature is proved to make a great difference to the degree of graphitization of CNFs and crystallinity of molybdenum carbide NPs, the HER activity of Pt/α-MoC_{1-x}-CNFs

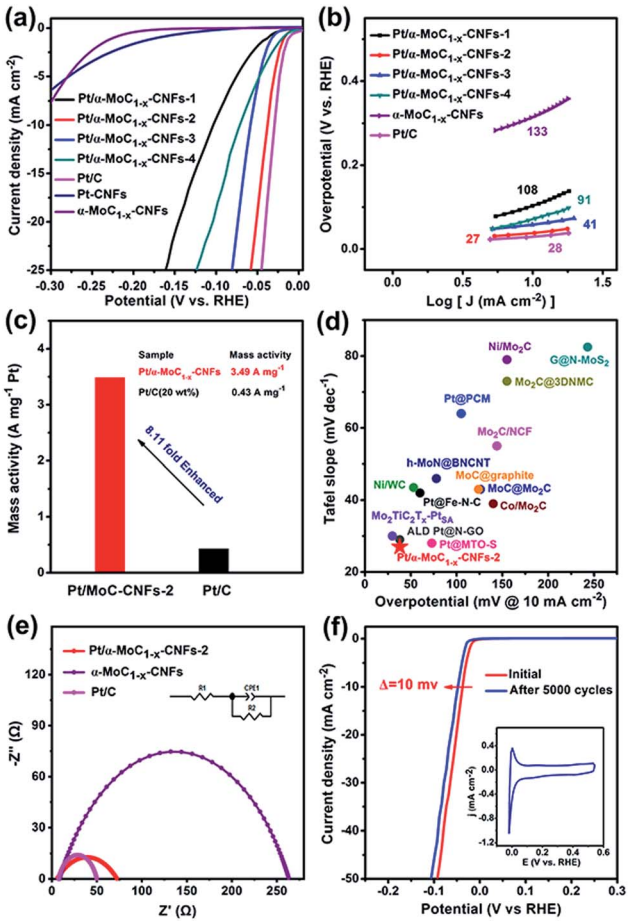

Fig. 5 Electrocatalytic performance of Pt/α-MoC_{1-x}-CNFs and reference HER catalysts. (a) HER polarization curves of α-MoC_{1-x}-CNFs, Pt-CNFs, Pt/C (20 wt%), Pt/α-MoC_{1-x}-CNFs-1, Pt/α-MoC_{1-x}-CNFs-2, Pt/α-MoC_{1-x}-CNFs-3 and Pt/α-MoC_{1-x}-CNFs-4, acquired using a graphite rod as the counter electrode in 0.5 M H_2SO_4 solution. (b) Corresponding Tafel slopes derived from (a). (c) The mass activity of commercial Pt/C and produced Pt/α-MoC_{1-x}-CNFs-2. (d) Comparison of the Tafel slope and overpotential (10 mA cm^{-2}) for various transition metal or Pt-based HER catalysts in 0.5 M H_2SO_4 solution. Values were plotted from references (Table S2†). (e) EIS Nyquist plots of α-MoC_{1-x}-CNFs, Pt/α-MoC_{1-x}-CNFs-2 and Pt/C (all the samples were tested at open circuit voltage). (f) Stability test of Pt/α-MoC_{1-x}-CNFs-2 through potential cycling, before and after 5000 cycles.

synthesized at different carbonization temperatures is also evaluated (Fig. S10a†). The η_{10} of all control samples exhibit a volcano curve with respect to the carbonization temperature: Pt/α-MoC_{1-x}-CNFs-800 (η_{10} = 133 mV), Pt/α-MoC_{1-x}-CNFs-900 (η_{10} = 73 mV), Pt/α-MoC_{1-x}-CNFs-1000 (η_{10} = 38 mV), Pt/α-MoC_{1-x}-CNFs-1100 (η_{10} = 50 mV), and Pt/α-MoC_{1-x}-CNFs-1200 (η_{10} = 68 mV). Higher carbonization temperature leads to inevitable agglomeration of NPs, thus the loss of active sites, while a low carbonization temperature is insufficient to generate qualified molybdenum carbide NPs. The optimal temperature (1000 °C) is feasible for the metastable property and moderate crystallinity of the α-MoC_{1-x} phase, generating a strong coupling and interaction with atomic Pt, thus a higher catalytic activity, which was proved by the XRD and

XPS analysis. Notably, with an even lower Tafel slope (21 mV dec^{-1}) shown in Fig. S10b,† Pt/α-MoC_{1-x}-CNFs-1100 presents a smaller overpotential compared with commercial Pt/C accompanied by large-current-density H_2 evolution ($j \geq 80$ mA cm^{-2}), indicating the outstanding inert reaction kinetics and continuous hydrogen evolution. To further evaluate the activity, the mass activity of Pt/α-MoC_{1-x}-CNFs-2 (1.5 wt% Pt) at an overpotential of 38 mV is normalized to be 3.49 A mg^{-1} (Fig. 5c), which is 8.11 times greater than that of commercial Pt/C (20 wt% Pt) at the same applied potential (0.43 A mg^{-1}). Considering the outstanding HER performance of Pt/α-MoC_{1-x}-CNFs, its overpotential and Tafel slop are benchmarked against recently reported research studies (Fig. 5d). Obviously, the impressive activity of Pt/α-MoC_{1-x}-CNFs-2 outperforms that of most transition metal based HER catalysts, such as Ni/WC[56] ($\eta_{10} = 53$ mV), MoC@graphite[29] ($\eta_{10} = 124$ mV), and Co/Mo_2C[27] ($\eta_{10} = 140$ mV). Meanwhile, the performance is also comparable or even superior to most atomic Pt based HER catalysts, such as Pt@Fe–N–C[53] ($\eta_{10} = 60$ mV, 2.1 wt% Pt), $Mo_2TiC_2T_x$-Pt_{SA}[57] ($\eta_{10} = 30$ mV, 1.2 wt% Pt), and ALD Pt@N-GO[58] ($\eta_{10} = 38$ mV, 2.1 wt% Pt). These values indicate that the ultrafine property of α-MoC_{1-x} NPs and highly efficient interaction between atomically doped Pt and α-MoC_{1-x} NPs undoubtedly maximize the catalytic sites and synergistic effect, thus boosting the HER activity as a result. To gain further insight into the electron transfer capability of Pt/α-MoC_{1-x}-CNFs, electrochemical impedance spectroscopy (EIS) has been performed and the results are shown in Fig. 5e and S11.† Compared to α-MoC_{1-x}-CNFs, Pt/α-MoC_{1-x}-CNFs-2 shows a much lower charge transfer resistance (R_{ct}), suggesting lower resistance and faster electron-transfer rate between the catalyst interface and electrolyte.

Long-term stability is another important criterion to assess the electrocatalytic performance. An accelerated test was conducted in an acid electrolyte by performing cyclic voltammetry (CV) between 0 and 0.54 V at a scan rate of 50 mV s^{-1}. As shown in the polarization curves of Pt/α-MoC_{1-x}-CNFs-2 before and after 5000 cycles (Fig. 5f), only 10 mV decay of the overpotential at 10 mA cm^{-2} is observed, indicating the excellent electrocatalytic durability. Moreover, after the continuous CV cycles, the one-dimensional nanostructure of CNF changes slightly (Fig. S12a and c†), while the NPs after the HER are well-maintained (Fig. S12b and d†), demonstrating that the active sites during the catalysis well survived even after the long-term test. The outstanding stability and durability can be attributed to the protection of CNFs over ultrafine Pt/α-MoC_{1-x} NPs and the intrinsic strong corrosion resistance of α-MoC_{1-x}.

Generally, the aforementioned method combining electrospinning with molecular interaction confinement has been used to fabricate Pt/α-MoC_{1-x}-CNF hybrid electrocatalysts. The conductive carbon nanofiber provides an ideal platform for electron/ion transport and acts as a protector over α-MoC_{1-x} NPs. The ultrafine α-MoC_{1-x} NPs not only offer abundant sites for coupling with atomic Pt, but also maximize the number of active sites. Moreover, the strong interaction between atomic Pt and α-MoC_{1-x} NPs is proved to greatly improve the intrinsic activity through electronic modulation. Adding the structure and electronic superiority together, the hybrid catalyst exhibits Pt-like catalytic kinetics towards the HER in acidic solution and the catalytic activity is superior to most advanced HER catalysts.

To prove the generality of this design and synthetic method to construct novel electrocatalysts, different materials such as Pt/(Fe-C_x)-CNFs, Ni/(W-C_x)-CNFs and Pt/W-C_x-CNFs (Fig. S13 and S14†) were also fabricated. Pt/W-C_x-CNFs were then taken as another example for further discussion. WC_x was investigated in previous research studies as a promising candidate to substitute noble metal as an efficient HER catalyst.[59,60] The way to prepare Pt/WC_x-CNFs is similar to that of Pt/α-MoC_{1-x}-CNFs except that PMA was replaced by PTA. Fig. 6a and b represent the typical SEM and TEM images of the as-obtained long-range uniform carbon nanofibers. As expected, no aggregation or big-sized NPs are observed. The selected-area electron diffraction (SAED) pattern shown in the inset in Fig. 6b confirms the relatively poor crystallinity of NPs, which may be beneficial to Pt atom embedding and stabilization in NPs. Further careful analysis reveals that densely ultrafine NPs with a mean size of 1.88 nm are well-dispersed on the surface of carbon nanofibers (Fig. 6c).

The properties of being highly dispersed and ultrafine are quite similar to Pt/α-MoC_{1-x}, which could increase the exposed active sites and help improve electrocatalytic performance. The HR-TEM image (Fig. S14†) shows that the lattice fringes of NPs are consistent with those of the W_2C structure, with a (101) lattice fringe spacing of 0.227 nm, while no lattice fringes of Pt are found. By comparing the HR-TEM of Pt/WC_x-CNFs and WC_x-CNFs (Fig. S15†), we found that the introduction of Pt did not transform the self-morphology of WC_x NPs. According to the information obtained above, it is highly possible to dope Pt into the WC_x NPs. The corresponding EDX mapping results reveal the uniform distribution of C, N, O, W and Pt in the as-synthesized Pt/WC_x-CNFs (Fig. S16†). The ICP result shows the

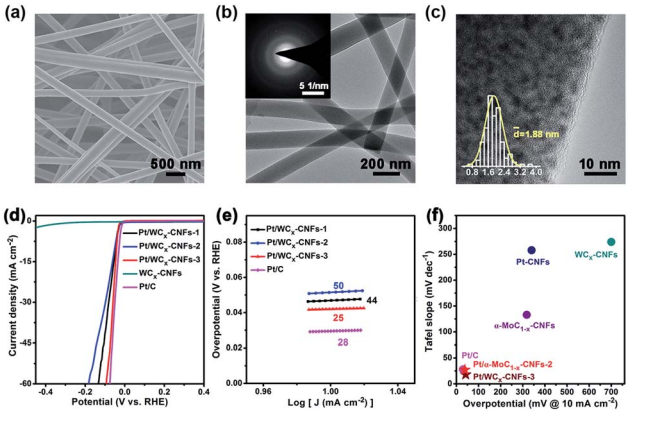

Fig. 6 (a) SEM image of Pt/WC_x-CNFs. (b) TEM image of Pt/WC_x-CNFs; the inset picture shows the SAED pattern of Pt/WC_x-CNFs. (c) HR-TEM image of Pt/WC_x-CNFs; the inset in (c) shows the size distribution of WC_x NPs. (d) HER polarization curves of bare WC_x-CNFs, Pt/C (20 wt%), Pt/WC_x-CNFs-1, Pt/WC_x-CNFs-2 and Pt/WC_x-CNFs-3 in 0.5 M H_2SO_4 solution. (e) Corresponding Tafel slopes derived from (d). (f) Comparison of the Tafel slope and overpotential (10 mA cm^{-2}) for catalysts in this paper in 0.5 M H_2SO_4 solution.

low content of Pt (2.4 wt%) in the hybrid catalyst. Through the XRD measurement (Fig. S17†), the main phase of W is confirmed. As for Pt/WC_x-CNFs, the characteristic diffraction peaks of W_2C and W are observed, which were commonly observed in WC_x catalysts.[61] No diffraction peaks of Pt can be found, indicating that Pt is doped in WC_x NPs, which is in accordance with the HR-TEM results.

The electrocatalytic HER activities of Pt/WC_x-CNFs with different molar ratios of $Pt(acac)_2$ and PTA were evaluated in 0.5 M H_2SO_4 solution. As shown in Fig. 6d, Pt/WC_x-CNFs-3 exhibits the lowest overpotential ($\eta_{10} = 42$ mV), slightly higher than that of Pt/α-MoC_{1-x}-CNFs-2 ($\eta_{10} = 38$ mV), while much better than that of WC_x-CNFs ($\eta_{10} > 500$ mV). The trend of catalytic activity again highlights the beneficial effects of Pt atom doping in WC_x NPs and synergistic reaction in boosting electrocatalytic activity. The corresponding Tafel plots of the as-prepared catalysts are presented in Fig. 6e. The Tafel slope of Pt/WC_x-CNFs-3 is 25 mV dec^{-1}, which is much smaller than that of WC_x-CNFs (274 mV dec^{-1}), suggesting faster HER kinetics. The superior HER kinetics of Pt/WC_x-CNFs-3 may originate from the strong synergistic effect between Pt atoms and WC_x NPs, which has been discussed in the mechanism of Pt/α-MoC_{1-x}-CNFs. The typical catalysts mentioned in this article are outlined in Table S1† and summarized in Fig. 6f in terms of the Tafel slope and η_{10}. It visually presents the enhanced activity of Pt-doped transition metal carbides, demonstrating the promotion between Pt and transition metal carbides simultaneously. The electron transfer capability of Pt/WC_x-CNFs was further probed by EIS (Fig. S18a†). By comparing the semicircles of Pt/WC_x-CNFs-3 and WC_x-CNFs, we found that the R_{ct} value of Pt/WC_x-CNFs-3 is much lower, implying quick electron transfer and advantageous HER kinetics towards the electrolyte interface. Notably, Pt/WC_x-CNFs-3 also presents excellent durability and stability (Fig. S18b†), with only 19 mV decay (η_{10}) after 5000 cycles shown in the polarization curves.

Conclusion

In summary, we have successfully produced ultrafine TMC NPs *in situ* formed on CNFs with atomic Pt *via* combining novel heteropoly acid mediation with an electrospinning strategy. The optimized electrocatalyst Pt/TMCs-CNFs presents excellent activity and durability towards the HER, which is mainly attributed to the following merits: (1) through confinement engineering of the nanostructure, both the ultrafine property of TMC NPs and atomic Pt doping contribute to the maximization of available active sites; (2) by means of heteroatom doping, the electron transfer between Pt and TMCs is illustrated, providing a synergetic effect towards the absorption ability, thus significantly increasing the intrinsic activity; (3) the conductive carbon nanofiber provides an ideal platform for electron/ion transport and also provides stable protection over the active sites. Such a synergistic structure simultaneously endows these hybrid catalysts with efficient and stable capability towards hydrogen evolution in acidic medium. The strategy in this paper not only improved the synthesis method of metal carbides, but also opened up a new engineering strategy for regulating the composition and nanostructure *via* molecular level confinement. Further studies of this synthetic strategy are currently underway in our group to investigate its wider applications.

Conflicts of interest

There are no conflicts to declare.

Acknowledgements

This work was supported by the National Natural Science Foundation of China (NSFC) (51573166, 51803077, 21905115, 11805139), the Natural Science Foundation of Jiangsu Province (BK20180627), the China Postdoctoral Science Foundation (2018M630517), the MOE & SAFEA, 111 Project (B13025), the national first-class discipline program of Light Industry Technology and Engineering (LITE2018-19), and the Fundamental Research Funds for the Central Universities (JUSRP11929). We also thank Prof. Zheng Jiang and Dr Hao Zhang (BL14W1), Shanghai Synchrotron Radiation Facility (SSRF), for excellent technical support and valuable discussion. The project was also supported by the Soochow University-Western University Centre for Synchrotron Radiation Research.

References

1 Y. Zheng, Y. Jiao, A. Vasileff and S. Z. Qiao, *Angew. Chem., Int. Ed.*, 2018, **57**, 7568–7579.
2 Q. Xue, M. Wu, X. C. Zeng and P. Jena, *J. Mater. Chem. A*, 2018, **6**, 9280.
3 F. Bu, W. Chen, M. F. Aly Aboud, I. Shakir, J. Gu and Y. Xu, *J. Mater. Chem. A*, 2019, **7**, 14526–14535.
4 Y. Wu, F. Li, W. Chen, Q. Xiang, Y. Ma, H. Zhu, P. Tao, C. Song, W. Shang, T. Deng and J. Wu, *Adv. Mater.*, 2018, **30**, 1803151.
5 X. Liu, Y. Jiao, Y. Zheng, K. Davey and S. Z. Qiao, *J. Mater. Chem. A*, 2019, **7**, 3648–3654.
6 L. Zhang, K. Doyle-Davis and X. Sun, *Energy Environ. Sci.*, 2019, **12**, 492–517.
7 Y. Qu, B. Chen, Z. Li, X. Duan, L. Wang, Y. Lin, T. Yuan, F. Zhou, Y. Hu, Z. Yang, C. Zhao, J. Wang, C. Zhao, Y. Hu, G. Wu, Q. Zhang, Q. Xu, B. Liu, P. Gao, R. You, W. Huang, L. Zheng, L. Gu, Y. Wu and Y. Li, *J. Am. Chem. Soc.*, 2019, **141**, 4505–4509.
8 Y. Jiang, X. Wu, Y. Yan, S. Luo, X. Li, J. Huang, H. Zhang and D. Yang, *Small*, 2019, **15**, 1805474.
9 P. Gandeepan, T. Muller, D. Zell, G. Cera, S. Warratz and L. Ackermann, *Chem. Rev.*, 2019, **119**, 2192–2452.
10 W. Pei, S. Zhou, Y. Bai and J. Zhao, *Carbon*, 2018, **133**, 260–266.
11 H. Sun, Z. Yan, F. Liu, W. Xu, F. Cheng and J. Chen, *Adv. Mater.*, 2020, **32**, 1806326.
12 X. Zang, W. Chen, X. Zou, J. N. Hohman, L. Yang, B. Li, M. Wei, C. Zhu, J. Liang, M. Sanghadasa, J. Gu and L. Lin, *Adv. Mater.*, 2018, **30**, 1805188.
13 Y. Zhu, G. Chen, Y. Zhong, W. Zhou and Z. Shao, *Adv. Sci.*, 2018, **5**, 1700603.

14 J. Miao, Z. Lang, X. Zhang, W. Kong, O. Peng, Y. Yang, S. Wang, J. Cheng, T. He, A. Amini, Q. Wu, Z. Zheng, Z. Tang and C. Cheng, *Adv. Funct. Mater.*, 2019, **29**, 1805893.
15 W. Chen, Y. Qu, L. Yao, X. Hou, X. Shi and H. Pan, *J. Mater. Chem. A*, 2018, **6**, 8021–8029.
16 D. Zhu, J. Liu, Y. Zhao, Y. Zheng and S. Z. Qiao, *Small*, 2019, **15**, 1805511.
17 J. X. Feng, S. Y. Tong, Y. X. Tong and G. R. Li, *J. Am. Chem. Soc.*, 2018, **140**, 5118–5126.
18 E. Hu, Y. Feng, J. Nai, D. Zhao, Y. Hu and X. W. Lou, *Energy Environ. Sci.*, 2018, **11**, 872–880.
19 Q. Gao, W. Zhang, Z. Shi, L. Yang and Y. Tang, *Adv. Mater.*, 2019, **31**, 1802880.
20 H. Vrubel and X. Hu, *Angew. Chem., Int. Ed.*, 2012, **51**, 12703–12706.
21 Q. Gao, W. Zhang, Z. Shi, L. Yang and Y. Tang, *Adv. Mater.*, 2019, **31**, 1970009.
22 J. Lin, J. Xu, W. Zhao, W. Dong, R. Li, Z. Zhang and F. Huang, *ACS Appl. Mater. Interfaces*, 2019, **11**, 19977–19985.
23 F. G. Baddour, C. P. Nash, J. A. Schaidle and D. A. Ruddy, *Angew. Chem., Int. Ed.*, 2016, **55**, 9026–9029.
24 Q. Hu, X. Liu, B. Zhu, L. Fan, X. Chai, Q. Zhang, J. Liu, C. He and Z. Lin, *Nano Energy*, 2018, **50**, 212–219.
25 H. Jiang and J. Caro, *Chem*, 2017, **3**, 209–210.
26 T. Ouyang, A. N. Chen, Z. Z. He, Z. Q. Liu and Y. Tong, *Chem. Commun.*, 2018, **54**, 9901–9904.
27 H. Lin, N. Liu, Z. Shi, Y. Guo, Y. Tang and Q. Gao, *Adv. Funct. Mater.*, 2016, **26**, 5590–5598.
28 H. Lin, Z. Shi, S. He, X. Yu, S. Wang, Q. Gao and Y. Tang, *Chem. Sci.*, 2016, **7**, 3399–3405.
29 Z. Shi, Y. Wang, H. Lin, H. Zhang, M. Shen, S. Xie, Y. Zhang, Q. Gao and Y. Tang, *J. Mater. Chem. A*, 2016, **4**, 6006–6013.
30 Y. Huang, Q. Gong, X. Song, K. Feng, K. Nie, F. Zhao, Y. Wang, M. Zeng, J. Zhong and Y. Li, *ACS Nano*, 2016, **10**, 11337–11343.
31 Y. Wang, L. Chen, X. Yu, Y. Wang and G. Zheng, *Adv. Energy Mater.*, 2017, **7**, 1601390.
32 X. Han, X. Wu, Y. Deng, J. Liu, J. Lu, C. Zhong and W. Hu, *Adv. Energy Mater.*, 2018, **8**, 1870110.
33 Y. Qiu, Z. Wen, C. Jiang, X. Wu, R. Si, J. Bao, Q. Zhang, L. Gu, J. Tang and X. Guo, *Small*, 2019, **15**, 1900014.
34 Z. Xing, C. Han, D. Wang, Q. Li and X. Yang, *ACS Catal.*, 2017, **7**, 7131–7135.
35 S. Li, J. Liu, Z. Yin, P. Ren, L. Lin, Y. Gong, C. Yang, X. Zheng, R. Cao, S. Yao, Y. Deng, X. Liu, L. Gu, W. Zhou, J. Zhu, X. Wen, B. Xu and D. Ma, *ACS Catal.*, 2019, **10**, 907–913.
36 D. Gohl, A. Garg, P. Paciok, K. J. J. Mayrhofer, M. Heggen, Y. Shao-Horn, R. E. Dunin-Borkowski, Y. Roman-Leshkov and M. Ledendecker, *Nat. Mater.*, 2019, DOI: 10.1038/s41563-019-0555-5.
37 D. A. Kuznetsov, Z. Chen, P. V. Kumar, A. Tsoukalou, A. Kierzkowska, P. M. Abdala, O. V. Safonova, A. Fedorov and C. R. Muller, *J. Am. Chem. Soc.*, 2019, **141**, 17809–17816.
38 X. Li, X. Yang, Y. Huang, T. Zhang and B. Liu, *Adv. Mater.*, 2019, **31**, 1902031.
39 Y. Wang, M. Wang, Z. Zhang, Q. Wang, Z. Jiang, M. Lucero, X. Zhang, X. Li, M. Gu, Z. Feng and Y. Liang, *ACS Catal.*, 2019, **9**, 6252–6261.
40 X. P. Yin, H. J. Wang, S. F. Tang, X. L. Lu, M. Shu, R. Si and T. B. Lu, *Angew. Chem., Int. Ed.*, 2018, **57**, 9382–9386.
41 S. Ye, F. Luo, Q. Zhang, P. Zhang, T. Xu, Q. Wang, D. He, L. Guo, Y. Zhang, C. He, X. Ouyang, M. Gu, J. Liu and X. Sun, *Energy Environ. Sci.*, 2019, **12**, 1000–1007.
42 W. Chen, J. Pei, C. T. He, J. Wan, H. Ren, Y. Wang, J. Dong, K. Wu, W. C. Cheong, J. Mao, X. Zheng, W. Yan, Z. Zhuang, C. Chen, Q. Peng, D. Wang and Y. Li, *Adv. Mater.*, 2018, **30**, 1800396.
43 B. Zhang, G. Sun, S. Ding, H. Asakura, J. Zhang, P. Sautet and N. Yan, *J. Am. Chem. Soc.*, 2019, **141**, 8185–8197.
44 H. Zhu, J. Zhang, R. Yanzhang, M. Du, Q. Wang, G. Gao, J. Wu, G. Wu, M. Zhang and B. Liu, *Adv. Mater.*, 2015, **27**, 4752–4759.
45 H. Zhu, L. Gu, D. Yu, Y. Sun, M. Wan, M. Zhang, L. Wang, L. Wang, W. Wu and J. Yao, *Energy Environ. Sci.*, 2017, **10**, 321–330.
46 H. Zhu, G. Gao, M. Du, J. Zhou, K. Wang, W. Wu, X. Chen, Y. Li, P. Ma and W. Dong, *Adv. Mater.*, 2018, **30**, 1707301.
47 B. Zhang, H. Asakura, J. Zhang, J. Zhang, S. De and N. Yan, *Angew. Chem., Int. Ed.*, 2016, **55**, 8319–8323.
48 L. Lin, W. Zhou, R. Gao, S. Yao, X. Zhang, W. Xu, S. Zheng, Z. Jiang, Q. Yu, Y. W. Li, C. Shi, X. D. Wen and D. Ma, *Nature*, 2017, **544**, 80–83.
49 D. S. Baek, G. Y. Jung, B. Seo, J. C. Kim, H. W. Lee, T. J. Shin, H. Y. Jeong, S. K. Kwak and S. H. Joo, *Adv. Funct. Mater.*, 2019, **29**, 1901217.
50 W. Han, L. Chen, B. Ma, J. Wang, W. Song, X. Fan, Y. Li, F. Zhang and W. Peng, *J. Mater. Chem. A*, 2019, **7**, 4734–4743.
51 X. Shi, A. Wu, H. Yan, L. Zhang, C. Tian, L. Wang and H. Fu, *J. Mater. Chem. A*, 2018, **6**, 20100–20109.
52 B. Qiao, A. Wang, X. Yang, L. F. Allard, Z. Jiang, Y. Cui, J. Liu, J. Li and T. Zhang, *Nat. Chem.*, 2011, **3**, 634.
53 X. Zeng, J. Shui, X. Liu, Q. Liu, Y. Li, J. Shang, L. Zheng and R. Yu, *Adv. Energy Mater.*, 2018, **8**, 1701345.
54 J. Diao, W. Yuan, Y. Su, Y. Qiu and X. Guo, *Adv. Mater. Interfaces*, 2018, **5**, 1800223.
55 H. J. Song, M. C. Sung, H. Yoon, B. Ju and D. W. Kim, *Adv. Sci.*, 2019, **6**, 1802135.
56 Y. Y. Ma, Z. L. Lang, L. K. Yan, Y. H. Wang, H. Q. Tan, K. Feng, Y. J. Xia, J. Zhong, Y. Liu, Z. H. Kang and Y. G. Li, *Energy Environ. Sci.*, 2018, **11**, 2114–2123.
57 J. Zhang, Y. Zhao, X. Guo, C. Chen, C. L. Dong, R. S. Liu, C. P. Han, Y. Li, Y. Gogotsi and G. Wang, *Nat. Catal.*, 2018, **1**, 985–992.
58 N. Cheng, S. Stambula, D. Wang, M. N. Banis, J. Liu, A. Riese, B. Xiao, R. Li, T. K. Sham, L. M. Liu, G. A. Botton and X. Sun, *Nat. Commun.*, 2016, **7**, 13638.
59 X. F. Lu, L. Yu, J. Zhang and X. W. Lou, *Adv. Mater.*, 2019, **31**, 1900699.
60 B. Xiong, W. Zhao, L. Chen and J. Shi, *Adv. Funct. Mater.*, 2019, **29**, 1902505.
61 Y. Hu, B. Yu, M. Ramadoss, W. Li, D. Yang, B. Wang and Y. Chen, *ACS Sustainable Chem. Eng.*, 2019, **7**, 10016–10024.